High-Q HF Microelectromechanical Filters

Frank D. Bannon, III, *Student Member, IEEE*, John R. Clark, *Student Member, IEEE*, and Clark T.-C. Nguyen, *Member, IEEE*

***Abstract*—IC-compatible microelectromechanical intermediate frequency filters using integrated resonators with Q's in the thousands to achieve filter Q's in the hundreds have been demonstrated using a polysilicon surface micromachining technology. These filters are composed of two clamped–clamped beam micromechanical resonators coupled by a soft flexural-mode mechanical spring. The center frequency of a given filter is determined by the resonance frequency of the constituent resonators, while the bandwidth is determined by the coupling spring dimensions and its location between the resonators. Quarter-wavelength coupling is required on this microscale to alleviate mass loading effects caused by similar resonator and coupler dimensions. Despite constraints arising from quarter-wavelength design, a range of percent bandwidths is still attainable by taking advantage of low-velocity spring attachment locations. A complete design procedure is presented in which electromechanical analogies are used to model the mechanical device via equivalent electrical circuits. Filter center frequencies around 8 MHz with Q's from 40 to 450 (i.e., percent bandwidths from 0.23 to 2.5%), associated insertion losses less than 2 dB, and spurious-free dynamic ranges around 78 dB are demonstrated using low-velocity designs with input and output termination resistances on the order of 12 kΩ.**

***Index Terms*—Bandpass, filter, high-Q, IF, insertion loss, MEMS, micromechanical.**

I. Introduction

THE MAJORITY of the high-Q bandpass filters commonly used in the radio frequency (RF) and intermediate frequency (IF) stages of heterodyning transceivers are realized using off-chip, mechanically resonant components, such as crystal filters and surface acoustic wave (SAW) devices. Due to higher quality factor Q, such technologies greatly outperform comparable filters implemented using transistor technologies, in insertion loss, percent bandwidth, and achievable rejection [1]–[4]. However, being off-chip components, these mechanical devices must interface with integrated electronics at the board level, and this constitutes an important bottleneck to miniaturization and performance of superheterodyne transceivers. For this reason, recent attempts to achieve single-chip transceivers for paging and cellular applications have utilized alternative architectures (e.g., direct-conversion [5], wideband-IF [6], or direct subsampling [7]), rather than superheterodyne, and so far, have often suffered in overall performance as a result.

Manuscript received April 13, 1999; revised September 1, 1999. This work was supported by the Defense Advanced Research Projects Agency and the National Science Foundation under Grants.

F. D. Bannon, III, was with the University of Michigan, Ann Arbor, MI 48109-2122 USA. He is now with Lucent Technologies, Holmdel, NJ 07733 USA (e-mail: bannon@lucent.com).

J. R. Clark and C. T.-C. Nguyen are with the University of Michigan, Ann Arbor, MI 48109-2122 USA (e-mail: jrclark@engin.umich.edu; ctnguyen@eecs.umich.edu).

Publisher Item Identifier S 0018-9200(00)02657-3.

Micromachining technologies that make possible high-Q on-chip micromechanical resonators [8], [9] now suggest a method for miniaturizing and integrating highly selective filters alongside transistors, with the intent of perhaps someday enabling miniaturized superheterodyne transceivers. With Q's of more than 80 000 [10] under vacuum and center frequency temperature coefficients in the range of -10 ppm/°C (several times less with nulling techniques) [11], polycrystalline silicon micromechanical resonators (abbreviated "μresonators") can potentially serve well as miniaturized substitutes for crystals in a variety of high-Q oscillator and filtering applications [10], [12], [13]. Previously, MF (i.e., 455 kHz), three-resonator prototypes of such filters have been demonstrated [14], [20]. For use in communications, however, much higher frequencies must be achieved. This work achieves frequency extension to the high-frequency (HF) range and reports on the design, fabrication, and performance of prototype, planar IC-processed, two-resonator μmechanical bandpass filters with center frequencies in the vicinity of 8 MHz, percent bandwidths on the order of 0.2% with associated insertion losses of less than 2 dB, stopband rejections greater than 35 dB, and spurious-free dynamic ranges (SFDR's) for offset tones 200 and 400 kHz away of 78 dB. Beginning with a qualitative description of micromechanical filter structure and operation in Section II, this paper continues with details on high-frequency micromechanical resonator design in Section III, then proceeds with a step-by-step description of micromechanical filter design in Section IV. Fabrication, design specifics, and performance test results are then presented in Sections V and VI, followed by projections on the ultimate frequency range of μmechanical filters in Section VII.

II. Qualitative Description of Filter Structure and Operation

Fig. 1 presents the perspective view schematic of a two-resonator filter, along with appropriate bias, excitation, and sensing circuitry. As shown, the filter consists of two identical μmechanical clamped–clamped beam resonators, coupled mechanically by a flexural-mode beam, all suspended 1300 Å above the substrate. Conducting strips underlie the central regions of each resonator and serve as capacitive transducer electrodes positioned to induce resonator vibration in a direction perpendicular to the substrate. The resonator-to-electrode gaps are targeted for 1300 Å.

Fig. 1(b) explicitly equates the actual filter to an equivalent mechanical circuit, in which each resonator is represented by a mass-spring-damper system, while the coupling beam corresponds to a network of mechanical springs. Such a coupled two-resonator system exhibits two mechanical resonance modes

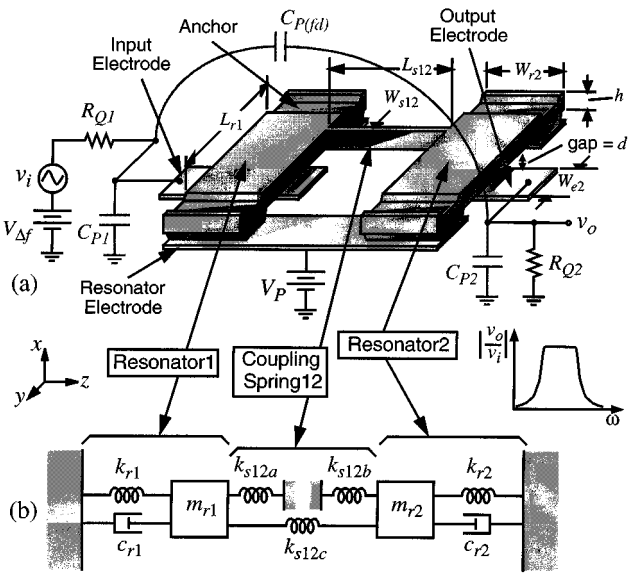

Fig. 1. (a) Perspective view schematic of a two-resonator μmechanical filter, along with the preferred bias, excitation, and sensing circuitry. Significant parasitic elements are also shown in gray. (b) The equivalent mechanical circuit.

with closely spaced frequencies that define the filter passband. The center frequency of the filter is determined primarily by the frequencies of the constituent resonators, while the spacing between modes (i.e., the bandwidth) is determined largely by the stiffness of the coupling spring. As shown in Fig. 2, each mode peak corresponds to a distinct, physical mode shape: In the lower frequency mode, both resonators vibrate in phase; and in the higher frequency mode, the resonators are 180° out of phase. As will be described, properly chosen termination resistors R_{Qn} are utilized to flatten the jagged passband shown in Fig. 2 to achieve that shown in Fig. 1.

To operate this filter, a dc-bias V_P is applied to the suspended filter structure, and an ac input voltage v_i is applied through resistor R_{Q1} to the input electrode (electrode 1), as shown in Fig. 1(a). The application of this input creates an x-directed electrostatic force between electrode 1 and the conductive resonator that induces x-directed vibration of the input resonator when the frequency of the input voltage comes within the passband of the mechanical filter. This vibrational energy is imparted to the output resonator via the coupling spring, causing it to vibrate as well. Vibration of the output resonator creates a dc-biased, time-varying capacitor between the conductive resonator and output electrode, which then sources an output current given by

$$i_{x2} = V_{\mathrm{Pn}} \frac{\partial C_2}{\partial x} \frac{\partial x}{\partial t} \tag{1}$$

where x is vertical displacement, $V_{\mathrm{Pn}} = V_P - V_n$ with V_n equal to the dc voltage on electrode n, and $\partial C_2/\partial x$ is the change in resonator-to-electrode capacitance per unit displacement at port 2. The current i_{x2} is then directed to resistor R_{Q2}, which converts the current to an output voltage v_o and, along with R_{Q1}, provides the proper termination impedance required to flatten the jagged passband of Fig. 2.

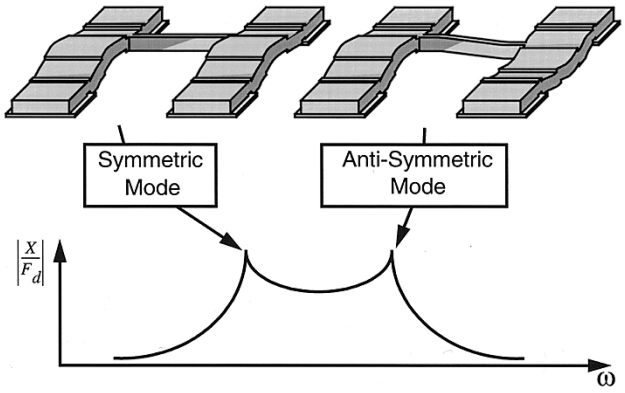

Fig. 2. Filter mode shapes and their correspondence to specific peaks in the unterminated frequency characteristic.

In effect, this device takes an electrical input signal, converts it to a mechanical signal, processes it in the mechanical domain, then reconverts the resulting signal to an electrical output signal, ready for further processing by subsequent electronic stages.

III. HF Micromechanical Resonators

Because the center frequency of a given mechanical filter is determined primarily by the resonance frequencies of its constituent resonators, careful mechanical resonator design is imperative for successful filter implementation. The selected μresonator design must not only be able to achieve the needed frequency but must also do so with adequate linearity and tunability, and with sufficient Q.

For many sensor applications, such as accelerometers [15] or gyroscopes [16], the lower the resonance frequency of the mechanical structure, the better the sensitivity of the device. Thus, the majority of previous micromachined mechanical devices aimed at sensor applications have been designed to resonate at very low frequencies, below 100 kHz. Designs with long spring lengths and large masses are common for these applications, and techniques that extend linearity and displacement amplitude, such as interdigitated comb-capacitive transducers and folded-beam suspensions [9], are often used.

Such designs, however, are impractical for applications in the HF range, and beyond. In order to maximize resonance frequency, governed by the general expression

$$f_0 = \frac{1}{2\pi}\sqrt{\frac{k_r}{m_r}} \tag{2}$$

the effective resonator spring stiffness k_r must be maximized, while its effective mass m_r is minimized. The optimum HF resonator design should thus avoid the increased mass of a comb structure and the stiffness reduction of a folded-flexure. For this reason, this work utilizes the simple clamped-clamped beam resonator shown in Fig. 3 under a typical bias and excitation configuration.

The resonance frequency of this clamped-clamped beam depends upon many factors, including geometry, structural material properties, stress, the magnitude of the applied dc-bias voltage V_P, and surface topography. Accounting for these while

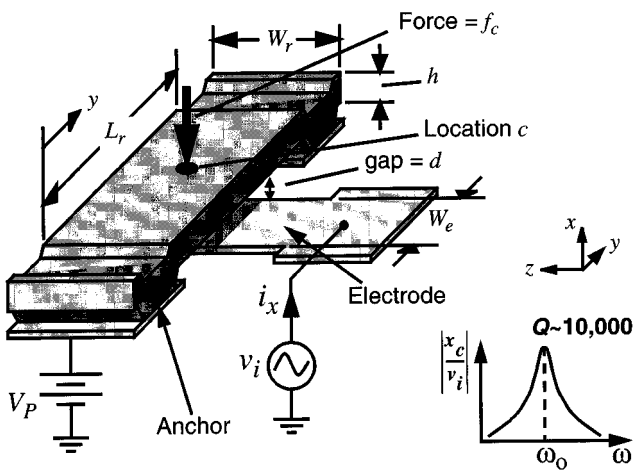

Fig. 3. Perspective view schematic of a clamped–clamped beam μmechanical resonator under a typical bias and excitation configuration. Note the mechanical input force f_c.

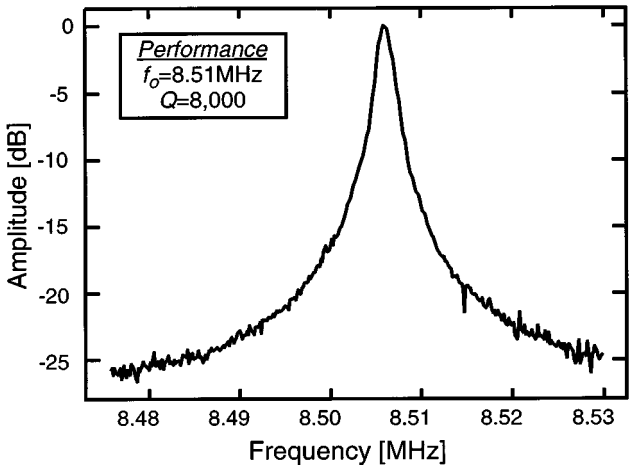

Fig. 4. Frequency characteristic for an 8.5-MHz polysilicon μmechanical resonator measured under 70-mTorr vacuum using a dc-bias voltage $V_P = 10$ V, a drive voltage of $v_i = 3$ mV, and a transresistance amplifier with a gain of 33 kΩ to yield an output voltage v_o. Amplitude = v_o/v_i.

neglecting finite width effects, an expression for resonance frequency can be written as

$$f_0 = f_{\text{nom}}[1 - g(d, V_P)]^{1/2}, \quad f_{\text{nom}} = 1.03\kappa\sqrt{\frac{E}{\rho}}\frac{h}{L_r^2} \quad (3)$$

where E and ρ are the Young's modulus and density of the structural material, respectively; h and L_r are specified in Fig. 3; f_{nom} is the nominal mechanical resonance frequency of the resonator if there were no electrodes or applied voltages; the function $g$models the effect of an electrical spring stiffness k_e that appears when electrodes and voltages are introduced and that subtracts from the mechanical stiffness k_m; and κ is a scaling factor that models the effects of surface topography (seen in Figs. 12 and 13). For the μresonators of this work, κ is dominated by anchor step-up and finite elasticity effects [17], [18], which are predictable using finite element analysis (FEA).

A. Electromechanical Operation

The resonators of this work utilize capacitive transduction mainly to simplify future integration with transistor circuits. For the described clamped–clamped beam vertically resonant design, the transducer capacitor is formed between the resonator beam and an underlying electrode, shown in Fig. 3. To actuate a given resonator, an input voltage, comprised of a dc-bias potential V_P and an ac signal v_i, is applied across the electrode-to-resonator transducer capacitor. (Note that the dc bias V_P is effectively being applied to one plate of a capacitor; there is no dc current associated with it, so no dc power consumption.) This combination of voltages generates an electrostatic force between the electrode and resonator, with the most dominant component at the frequency of v_i given by [9], [10]

$$F_d = V_P\frac{\partial C}{\partial x}v_i \quad (4)$$

where $\partial C/\partial x$ is the change in electrode-to-resonator capacitance per unit displacement of the resonator, approximately given by (neglecting fringing fields and static beam bending)

$$\frac{\partial C}{\partial x} = \frac{\varepsilon_0 W_r W_e}{d_0^2} \quad (5)$$

where d_0 is the electrode-to-resonator gap spacing under static (nonresonance) conditions. When the frequency of v_i matches the resonance frequency, the beam begins to vibrate with a zero-to-peak displacement amplitude at location y given by

$$x(y) = \frac{QF_d}{k_{\text{reff}}(y)} = \frac{Q}{k_{\text{reff}}(y)}V_P\frac{\partial C}{\partial x}v_i \quad (6)$$

creating a current i_x already described in association with (1). In (6), $k_{\text{reff}}(y)$ is an effective stiffness at location y to be determined later in this section via integration over the electrode width. When plotted versus input frequency, i_x traces out the bandpass biquad spectrum shown in Fig. 3. For the resonator design of this work (summarized in Table II), a typical vibration amplitude is 49 Å at the beam center for a dc bias of $V_P = 10$ V and an ac input voltage of $v_i = 3$ mV.

The frequency characteristic for an 8.5-MHz polysilicon μmechanical resonator, measured under linear drive conditions at 70 mTorr pressure via an experimental setup to be described in Section VI, is presented in Fig. 4. The quality factor Q extracted from this plot is 8000, which is plenty adequate for demonstration of low insertion loss filters. Note, however, that this Q is only achievable under vacuum, where viscous gas damping is minimized [19]. Much lower Q's on the order of hundreds are seen under atmospheric pressure.

B. Equivalent Lumped Parameter Mechanical Circuit

For the purposes of filter design, it is often convenient to define an equivalent lumped-parameter mass-spring-damper mechanical circuit for this resonator (see Fig. 1), with element values that vary with location on the resonator. With reference

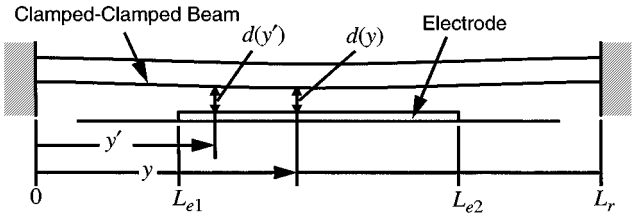

Fig. 5. Resonator cross-sectional schematic for frequency-pulling and impedance analysis.

to Fig. 5, the equivalent mass at a location y on the resonator is given by [20]

$$m_r(y) = \frac{KE_{\rm tot}}{(1/2)(v(y))^2} = \frac{\rho W_r h \int_0^{L_r} [X_{\rm mode}(y')]^2 (dy')}{[X_{\rm mode}(y)]^2} \tag{7}$$

where

$$X_{\rm mode}(y) = \zeta(\cos ky - \cosh ky) + (\sin ky - \sinh ky) \tag{8}$$

$k = 4.730/L_r$ and $\zeta = -1.01781$ for the fundamental mode, $KE_{\rm tot}$ is the peak kinetic energy in the system, $v(y)$ is the velocity at location y, and dimensional parameters are given in Fig. 5. The equivalent spring stiffness follows readily from (2) and (7) and is given by

$$k_r(y) = \omega_0^2 m_r(y) \tag{9}$$

where ω_0 is the radian resonance frequency of the beam. Last, the damping factor is given by

$$c_r(y) = \frac{\sqrt{k_m(y) m_r(y)}}{Q_{\rm nom}} = \frac{\omega_{\rm nom} m_r(y)}{Q_{\rm nom}} = \frac{k_m(y)}{\omega_{\rm nom} Q_{\rm nom}} \tag{10}$$

where

$$k_m(y) = \omega_{\rm nom}^2 m_r(y) \tag{11}$$

is the mechanical stiffness of the resonator alone, without the influence of applied voltages and electrodes to be discussed next, and $Q_{\rm nom}$ is the quality factor of the resonator under the same conditions.

C. Voltage-Tunable Electrical Stiffness

As indicated in (3), where g is seen to be a function of dc-bias voltage V_P, the resonance frequency of this device is tunable via adjustment of V_P [8], and this can be used advantageously to implement filters with tunable center frequencies, or to correct for passband distortion caused by finite planar fabrication tolerances. The dc-bias dependence of resonance frequency arises from a V_P-dependent electrical spring constant k_e that subtracts from the mechanical spring constant of the system k_m, lowering the overall spring stiffness $k_r = k_m - k_e$, thus lowering the resonance frequency according to the expression

$$f_0 = \frac{1}{2\pi}\sqrt{\frac{k_m - k_e}{m_r}} = \frac{1}{2\pi}\sqrt{\frac{k_m}{m_r}}\left[1 - \left\langle \frac{k_e}{k_m} \right\rangle\right]^{1/2}$$
$$= 1.03\kappa\sqrt{\frac{E}{\rho}}\frac{h}{L^2}\left[1 - \left\langle \frac{k_e}{k_m} \right\rangle\right]^{1/2} \tag{12}$$

where k_m and m_r denote values at a particular location (usually the beam center location), and the quantity $\langle k_e/k_m \rangle$ must be obtained via integration over the electrode width W_e due to the location dependence of k_m.

The electrical spring stiffness k_e is generated by the nonlinear dependence of electrode-to-resonator gap capacitance $C_n(x)$ on displacement x and is dependent very strongly upon the electrode-to-resonator gap spacing d. At a specific location y' centered on an infinitesimally small width of the electrode dy', the differential in electrical stiffness is given by [21]

$$dk_e(y') = V_P^2 \frac{\varepsilon_0 W_r dy'}{(d(y'))^3} \tag{13}$$

where the electrode-to-resonator gap distance d is now seen to also be location dependent, since the beam bends somewhat due to the dc bias V_P applied between the electrode and resonator. Recognizing that for the fundamental mode the static and dynamic stiffnesses are virtually the same, and assuming a static bending shape due to the distributed dc force defined by the function $X_{\rm static}(y)$, the gap distance can be expressed as

$$d(y) = d_0 - \frac{1}{2} V_P^2 \varepsilon_0 W_r \int_{L_{e1}}^{L_{e2}} \frac{1}{k_m(y')(d(y'))^2} \frac{X_{static}(y)}{X_{\rm static}(y')}\, dy' \tag{14}$$

where d_0 is the static electrode-to-resonator gap with $V_P = 0$ V. In (14), the second term represents the static displacement of the resonator towards the electrode at a particular location y, evaluated by integration over the width of the electrode, from $y = L_{e1}$ to L_{e2}. In this work the electrode is centered with the resonator beam center, and thus $L_{e1} = 0.5(L_r - W_e)$ and $L_{e2} = 0.5(L_r + W_e)$. Since the desired variable $d(y)$ appears on both sides of (14), one of them within an integral, (14) is best solved by first assuming $d(y) = d_0$ on the right side, solving for $d(y)$ on the left, then using this function again on the right, iterating until $d(y)$ converges. In addition, for most cases (14) is not overly sensitive to the function $X_{\rm static}(y)$, so $X_{\rm mode}(y)$ given by (8) can be substituted for $X_{\rm static}(y)$ with little difference. It should be noted that more rigorous versions of (14) are attainable through strict static analysis, but these often take the form of polynomial expansions and are less intuitive than (14).

The quantity $\langle k_e/k_m \rangle$ may now be found by integrating over the electrode width and is given by

$$\left\langle \frac{k_e}{k_m} \right\rangle = g(d, V_P) = \int_{L_{e1}}^{L_{e2}} \frac{dk_e(y')}{k_m(y')}. \tag{15}$$

Given the dependencies of (13)–(15), and assuming a set value of V_P, designing the resonator of Fig. 3 for a specific resonance frequency amounts to setting geometric dimensions L_r, W_r, and W_e via CAD layout, since all other variables are determined at the outset by fabrication technology.

D. Pull-In Voltage $V_{\rm PI}$

When the applied dc-bias voltage V_P is sufficiently large, catastrophic failure of the device ensues, in which the resonator beam is pulled down onto the electrode. This leads to either destruction of the device due to excessive current passing through the now shorted electrode-to-resonator path or at least a removal of functionality if a dielectric layer (e.g., an oxide or nitride) is

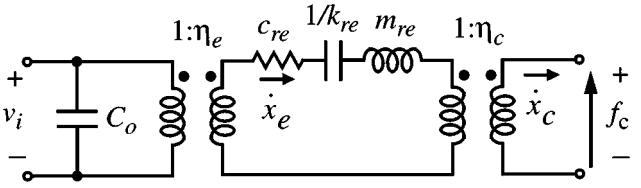

Fig. 6. Equivalent circuit for a μmechanical resonator with both electrical (voltage v_i) and mechanical (force f_c) inputs and outputs.

TABLE I
MECHANICAL-TO-ELECTRICAL CORRESPONDENCE IN THE CURRENT ANALOGY

Mechanical Variable	Electrical Variable
Damping, c	Resistance, R
Stiffness^{-1}, k^{-1}	Capacitance, C
Mass, m	Inductance, L
Force, f	Voltage, V
Velocity, v	Current, I

present above the electrode to prevent electrical contact between it and the conductive resonator beam.

Unlike previous low-frequency micromechanical structures [8], [15], the attractive electrostatic force between the electrode and this HF resonator that incites pulldown now acts against a very large distributed stiffness that must be integrated over the electrode area to accurately predict the pulldown voltage $V_{\rm PI}$. Thus, previously used closed-form expressions for $V_{\rm PI}$ [21] based on lumped parameter analysis are no longer applicable. Rather, for this resonator, the procedure for determining $V_{\rm PI}$ entails finding the V_P that sets the resonance frequency equal to zero, and thus, with reference to (12), amounts to setting (15) equal to unity and solving for the V_P variable.

E. Small-Signal Electrical Equivalent Circuit

To conveniently model and simulate the impedance behavior of this μmechanical resonator in an electromechanical circuit, an electrical equivalent circuit is needed [8], [22], [23]. As shown in Fig. 3, both electrical and mechanical inputs and outputs are possible for this device, so the equivalent circuit must be able to model both. In addition, for physical consistency from both transducer and noise perspectives, a circuit model that directly uses the lumped mechanical elements summarized by (7)–(10) is preferred. Fig. 6 presents the equivalent circuit used in this work, in which transformers model both electrical and mechanical couplings to and from the resonator, which itself is modeled by a core *LCR* circuit—the electrical analogy to a mass-spring-damper system—with element values corresponding to actual values of mass, stiffness, and damping as given by (7)–(10). In this circuit, the current electromechanical analogy is utilized, summarized in Table I.

When looking into the electrode port of the equivalent resonator circuit of Fig. 6, a transformed *LCR* circuit is seen, with element values given by

$$L_x = \frac{m_{\rm re}}{\eta_e^2} \quad C_x = \frac{\eta_e^2}{k_{\rm re}} \quad R_x = \frac{\sqrt{k_{\rm re} m_{\rm re}}}{Q\eta_e^2} = \frac{c_{\rm re}}{\eta_e^2} \tag{16}$$

where the subscript e denotes the electrode location at the very center of the resonator beam (i.e., at $y = L_r/2$). An expression for the electromechanical transformer turns ratio η_e can be obtained via an impedance analysis yielding the motional resistance R_x seen across the electrode-to-resonator gap at resonance. Pursuant to this, the voltage-to-displacement transfer function at a given location y (see Fig. 5) at resonance is first found using phasor forms of (4)—(6), (8), and (9) and integrating over the electrode width to yield

$$\frac{X}{V_i}(y) = \int_{L_{e1}}^{L_{e2}} \frac{QV_P\varepsilon_0 W_r}{[d(y')]^2 k_r(y')} \frac{X_{\rm mode}(y)}{X_{\rm mode}(y')}\, dy'. \tag{17}$$

Using the phasor form of (1), the series motional resistance seen looking into the drive electrode is then found to be

$$R_x = \frac{V_i}{I_x} = \left[\int_{L_{e1}}^{L_{e2}} \frac{\omega_0 V_P \varepsilon_0 W_r}{[d(y)]^2} \cdot \frac{X}{V_i}(y)\, dy\right]^{-1}. \tag{18}$$

Inserting (17), factoring out $c_{\rm re} = k_{\rm re}/(\omega_0 Q)$, and extracting η_e yields

$$\eta_e = \sqrt{\int_{L_{e1}}^{L_{e2}} \int_{L_{e1}}^{L_{e2}} \frac{V_P^2(\varepsilon_0 W_r)^2}{[d(y')d(y)]^2} \frac{k_{\rm re}}{k_r(y')} \frac{X_{\rm mode}(y)}{X_{\rm mode}(y')}\, dy'\, dy}. \tag{19}$$

Note that the effective integrated stiffness defined in (6) can also be extracted from (17), yielding

$$k_{\rm eff}(y) = \left[\int_{L_{e1}}^{L_{e2}} \left[\frac{d_0}{d(y')}\right]^2 \frac{1}{k_r(y')} \frac{1}{W_e} \frac{X_{\rm mode}(y)}{X_{\rm mode}(y')}\, dy'\right]^{-1}. \tag{20}$$

The transformer turns ratio η_c in Fig. 6 models the mechanical impedance transformation achieved by mechanically coupling to the resonator at a y location displaced from its center. As will be seen, such coupling will be required when implementing filters with two or more resonators. Expressed in terms of a stiffness ratio, the equation for the mechanical transformer turns ratio when coupling at a distance l_c from an anchor takes the form

$$\eta_c = \sqrt{\frac{k_r y = l_c}{k_{\rm re}}}. \tag{21}$$

Finally, for the equivalent circuit of Fig. 6, it should be noted that the damping constant c_r is not inherently a function of the electrical stiffness k_e. Thus, when expressed in terms of the overall stiffness k_r of the system, the Q of the resonator must be adjusted so that c_r retains its original value given by (10). In terms of k_r and ω_0, then, expressions for c_r take on the form

$$c_r = \frac{\omega_0 m_r}{Q} = \frac{k_r}{\omega_0 Q} = \frac{\sqrt{k_r m_r}}{Q} \tag{22}$$

where

$$Q = Q_{\rm nom}\left[1 - \left\langle \frac{k_e}{k_m} \right\rangle\right]^{1/2}. \tag{23}$$

Note that the effective resonator quality factor Q is dependent upon the electrical spring stiffness k_e, and thus is also a function of the dc-bias voltage V_P. In this paper, the variable Q denotes

that defined by (23), while $Q_{\rm nom}$ is reserved for zero-bias conditions.

IV. Filter Design

Despite the use of vibrating μmechanical resonators rather than transistor-based or *LCR* biquads, the network topologies for the mechanical filters of this work differ very little from those of their purely electronic counterparts, and in principal can be designed at the system level via a procedure derived from well-known, coupled resonator ladder filter synthesis techniques. In particular, given the equivalent *LCR* element values for a prototype μmechanical resonator, it is possible to synthesize a mechanical filter entirely in the electrical domain, converting to the mechanical domain only as the last step. However, although possible, such a procedure is not recommended, since knowledge and ease of design in both electrical and mechanical domains can greatly reduce the effort required.

The design procedure for the two-resonator micromechanical filter of this work can be itemized as follows.

1) Design and establish the μmechanical resonator prototype to be used, choosing necessary geometries for the needed frequency and insuring that enough electrode-to-resonator transducer coupling is provided to allow for predetermined termination resistor values.
2) Choose a manufacturable value of coupling beam width W_s and design coupling beam(s) corresponding to a "quarter-wavelength" of the filter center frequency.
3) Determine the coupling location(s) on the resonators corresponding to the filter bandwidth of interest.
4) Generate a complete equivalent circuit for the overall filter and verify the design using a circuit simulator.

Each of the above steps will now be expanded.

A. Micromechanical Resonator Design

The μmechanical resonators comprising the filter are preferably designed to be identical, each with the same stand-alone resonance frequency. Design equations governing the dimensions and bias voltages required to achieve a given frequency have already been presented in Section III.

In addition to determining the center frequency of the filter, the resonator design also dictates the termination resistors required for passband flattening. As with *LC*-ladder filters, the described μmechanical filters must be terminated with the proper impedance values. Without proper termination, the resonator Q's are too large, and the filter passband consists of distinct peaks of selectivity, as seen in Fig. 2. In order to flatten the passband between the peaks, the Q's of the constituent resonators (more precisely, of the end resonators) must be reduced, and this can be done by terminating the filter with resistors. In Fig. 1, resistors R_{Q1} and R_{Q2} serve this function. The required value of termination resistance for a μmechanical filter with center frequency f_0 and bandwidth B is given by

$$R_{\rm Qi} = \left(\frac{Q}{q_i Q_{\rm fltr}} - 1\right) R_{\rm xi} \tag{24}$$

where Q is the unloaded quality factor of the constituent resonators, $Q_{\rm fltr}$=f_0/B, i refers to the end resonator in question,

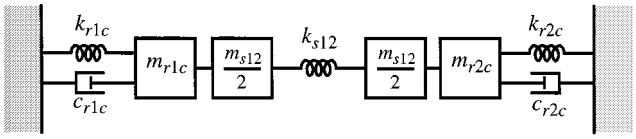

Fig. 7. Equivalent mechanical circuit for the two-resonator filter of Fig. 1(a) using a coupling beam of length less than an eighth of a wavelength of the operating frequency.

and q_i is a normalized q parameter obtained from a filter cookbook [24]. For the common case where $Q \gg Q_{\rm fltr}$, (24) becomes

$$R_{Qi} \cong \frac{\sqrt{k_{\rm rie} m_{\rm rie}}}{q_i Q_{\rm fltr} \eta_e^2} = \frac{k_{\rm rie}}{\omega_0 q_i Q_{\rm fltr} \eta_e^2}. \tag{25}$$

Of the variables in (25), the electromechanical coupling factor η_e is often the most convenient to adjust for a desired value of termination resistance. Thus, considering both (19) and (25), termination impedance $R_{\rm Qi}$ requirements and bias voltage V_P limitations often dictate the electrode-to-resonator gap spacing and overlap for a particular resonator design.

B. Coupling Beam Design

If each resonator is designed to have the same resonance frequency, then the passband of the overall filter will be centered around this frequency. The coupling spring acts to effectively pull the resonator frequencies apart, creating two closely spaced resonance modes that constitute the ends of the filter passband. For a given filter center frequency f_0 and bandwidth B, the required coupling beam spring constant can be found using the expression [20], [24]

$$k_{s12} = k_{\rm rc} \left(\frac{B}{f_0}\right) k_{12} \tag{26}$$

where $k_{\rm rc}$ is the resonator stiffness at the coupling location and k_{12} is the normalized coupling coefficient between resonator tanks for a given filter type (i.e., Butterworth, Chebyshev, etc.) [24]. The needed value of coupling spring constant k_{s12} is then attained by proper choice of coupling beam geometry using expressions to be determined.

The design of the coupling beam is complicated by the fact that the beam itself has finite mass. In particular, for the case of microscale filters, the coupling beam mass is on the same order as that of the resonator beams. Unless accounted for, this beam mass can add to the masses of the adjacent resonators, thereby changing their individual resonance frequencies as dictated by (2), and in turn, changing the center frequency of the filter or distorting its passband if it uses more than two resonators. This is depicted in Fig. 7, which shows a specific case where each resonator effectively takes on half the mass of the coupling spring, leading to an overall shift in filter center frequency as seen under simulation.

Although instructive, Fig. 7 actually only describes the special case where the coupling beam length is less than an eighth of the acoustic wavelength corresponding to the frequency of operation. For this special case, the coupling beam can be modeled by the lumped mass-spring system shown. In general, however, especially at high frequencies, the coupling beam is more accurately modeled by an acoustic transmission line—the

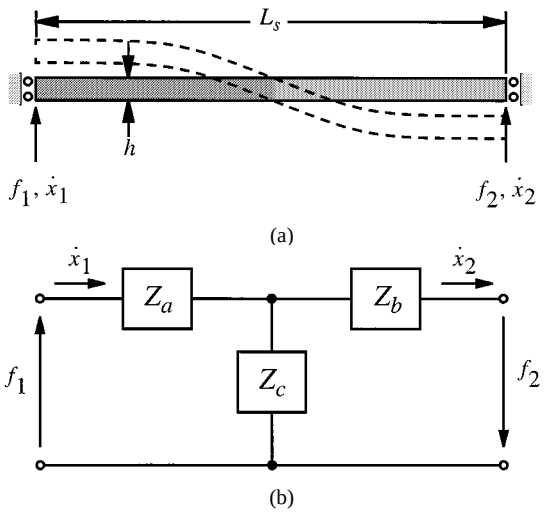

Fig. 8. (a) Coupling beam under forces f_1 and f_2 with corresponding velocity responses. (b) General transmission line T-model for the coupling beam.

mechanical analog to the familiar electrical transmission line. For this mechanical transmission line, a *distributed* mechanical circuit is more applicable, and the amount of coupling beam mass and stiffness effectively seen by the resonators adjacent to the coupling beam actually vary with the beam dimensions and the frequency of operation. For the purposes of filter design, Fig. 8 presents a general transmission line model for the coupling beam, consisting of a T network of mechanical impedances.

Pursuant to determination of the values of Z_a, Z_b, and Z_c in Fig. 8, the mechanical impedance behavior of the coupling beam as seen by the adjacent (attached) resonators can be conveniently modeled via an impedance matrix of the form [25]

$$\begin{bmatrix} f_1 \\ \dot{x}_1 \end{bmatrix} = \begin{bmatrix} \dfrac{H_6}{H_7} & -\dfrac{2EI_s\alpha^3H_1}{j\omega L_s^3H_7} \\ -\dfrac{j\omega L_s^3H_3}{EI_s\alpha^3H_7} & \dfrac{H_6}{H_7} \end{bmatrix} \begin{bmatrix} f_2 \\ \dot{x}_2 \end{bmatrix} = \begin{bmatrix} A & B \\ C & D \end{bmatrix} \begin{bmatrix} f_2 \\ \dot{x}_2 \end{bmatrix} \tag{27}$$

where

$$H_1 = \sinh\,\alpha \sin\,\alpha \tag{28}$$

$$H_3 = \cosh\,\alpha \cos\,\alpha - 1 \tag{29}$$

$$H_6 = \sinh\,\alpha \cos\,\alpha + \cosh\,\alpha \sin\,\alpha \tag{30}$$

$$H_7 = \sin\,\alpha + \sinh\,\alpha. \tag{31}$$

$\alpha = L_s(\rho W_s h\omega^2/(EI_s))^{0.25}$, $I_s = W_s h^3/12$, W_s is the width of the coupling beam, other needed dimensions are given in Fig. 8(a), and we have assumed that rotation of the coupling beam at the connection points is not significant. For cases where rotation is important, the matrix in (27) becomes larger [25] but the solution methods remain similar.

Equating the circuit of Fig. 8(b) to a chain network described by (27) [24], then solving for the series and shunt impedances in terms of chain matrix elements, yields

$$Z_a = Z_b = \frac{A-1}{C} = \frac{jEI_s\alpha^3(H_6 - H_7)}{\omega L_s^3 H_3} \tag{32}$$

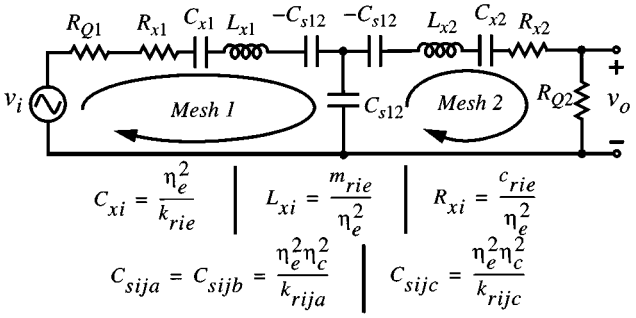

Fig. 9. Simplified equivalent circuit for the micromechanical filter of Fig. 1 using a quarter-wavelength coupling beam.

and

$$Z_c = \frac{1}{C} = \frac{jEI_s\alpha^3H_7}{\omega L_s^3 H_3}. \tag{33}$$

In order to minimize susceptibility to beam geometric variations (i.e., mass variations) caused by finite layout or fabrication tolerances, the coupling beam should be designed to correspond to a quarter-wavelength of the filter center frequency. This can be achieved by choosing coupling beam dimensions such that the series and shunt arm impedances of Fig. 8(b) take on equal and opposite values, and thus cancel in each mesh. By inspection of (32) and (33), Z_a and Z_c take on equal and opposite values when

$$H_6 = \sinh\,\alpha \cos\,\alpha + \cosh\,\alpha \sin\,\alpha = 0. \tag{34}$$

Using the selected value of W_s [in step 2) of Section IV] and assuming that h is set by technology, (34) can be solved for the L_s that corresponds to an effective quarter-wavelength of the operating frequency. With quarter-wavelength coupler dimensions, the impedances of Fig. 8(b) are given by

$$Z_a = Z_b = \frac{EI_sH_7}{j\omega L_s^3H_3} = \frac{k_{\rm sa}}{j\omega} \tag{35}$$

and

$$Z_c = -\frac{EI_sH_7}{j\omega L_s^3H_3} = \frac{k_{\rm sc}}{j\omega}. \tag{36}$$

From these equations, with the help of (29) and (31) for expansion purposes, the stiffness of a quarter-wavelength coupling beam is found to be

$$k_{\rm sc} = -k_{\rm sa} = -\frac{EI_s\alpha^3(\sin\,\alpha + \sinh\,\alpha)}{L_s^3(\cos\,\alpha\,\cosh\,\alpha - 1)}. \tag{37}$$

It should be noted that in addition to decreasing the overall filter susceptibility to variations in coupling beam geometry, the use of quarter-wavelength coupling beams also allows the use of identical resonators in the filter. This is perhaps best illustrated in the electrical domain, in the context of the simplified filter network shown in Fig. 9, obtained using the current electromechanical analogy of Table I on the lumped mechanical circuit of Fig. 1(b). Here, *LCR* circuits represent the resonators and a capacitive T-network models the coupling beam. As a result of filter synthesis, one property of this network is that each mesh with all others open-circuited must resonate at the center frequency of the filter f_0 [24]. Upon inspection of *Mesh*

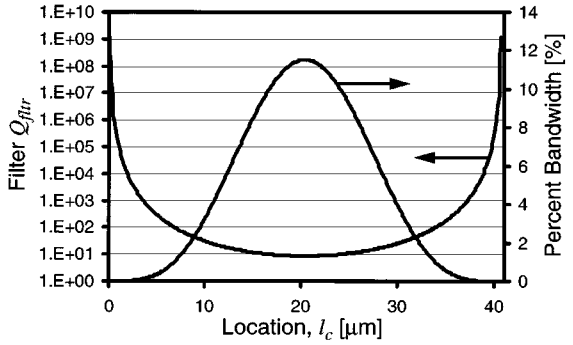

Fig. 10. Simulated plot of $Q_{\rm fltr}$ and percent bandwidth versus coupling location l_c along the length of a resonator beam.

1, with *Mesh* 2 open-circuited, the capacitors $C_{s12c} = C_{s12}$ and $C_{s12a} = -C_{s12}$ are seen to cancel, leaving only the L_x and C_x of the μmechanical resonator to contribute to the frequency of *Mesh* 1. The same applies for *Mesh* 2 with *Mesh* 1 open-circuited. Thus, when quarter-wavelength coupling beams are utilized, all of the resonators comprising the filter must be identical, each resonating at the center frequency of the filter.

The availability of designs using identical resonators is especially important for the case of the planar-fabricated micromechanical filters of this work, since matched resonators are much easier to achieve in a planar process than are resonators with varying, specific frequencies—i.e., matching tolerances are much better than absolute tolerances in planar processes.

C. Coupling Location (Low-Velocity Coupling)

The maximum overall filter quality factor ($Q_{\rm fltr} = f_0/B$) attainable via a mechanical filter is proportional to the ratio of the resonator and coupling beam spring constants $k_{\rm rc}/k_{s12}$ and is given by using (26)

$$Q_{\rm fltr} = \frac{1}{P_{\rm BW}} = k_{12}\left(\frac{k_{\rm rc}}{k_{s12}}\right) \tag{38}$$

where $P_{\rm BW}$ is percent bandwidth. For the case of *macroscopic* mechanical filters, $k_{\rm rc}/k_{s12}$ can be made quite large, because the resonators are often much bigger and thicker than their associated coupling springs [20]. On the other hand, in μmechanical filters, the resonators and couplers are usually of similar size, and thus, the ratio $k_{\rm rc}/k_{s12}$ is limited. This, then, limits the attainable $Q_{\rm fltr}$ (or percent bandwidth).

A novel method for attaining greater $Q_{\rm fltr}$ takes advantage of the fact that the dynamic spring constant $k_{\rm rc}$ of a clamped–clamped beam is larger at locations closer to the anchor points—i.e., it is larger at points moving with lower velocity at resonance. This can be seen easily from (7) and (9), which give resonator mass and stiffness as a function of beam location. Thus, by coupling the beams closer to the anchor points, rather than at the centers of resonator beams, higher $k_{\rm rc}/k_{s12}$ can be attained, and thus higher $Q_{\rm fltr}$ can be achieved, even when the resonators and coupling springs have similar sizes.

Fig. 10 illustrates this point with a plot of $Q_{\rm fltr}$ versus coupling location l_c along the length of a resonator beam. As shown, $Q_{\rm fltr}$ is highest near the anchor points where the velocity is lowest, and smallest at the beam center, where the velocity is maximized. Since $Q_{\rm fltr}$ is merely the reciprocal of percent bandwidth, Fig. 10 also shows that the bandwidth of the filter can be set by appropriately selecting the location at which the resonator and the coupling beam meet. This is a very convenient feature, since it allows the use of a set coupling beam geometry. In other words, the coupling beam need not be redesigned to accommodate filters with different bandwidths; only one quarter-wavelength coupling beam need be designed—with a specific length, width, and thickness—and filter bandwidth can be varied by changing only the resonator-to-coupler attachment location.

D. Equivalent Circuit and Design Verification

Although useful for the purpose at hand, Fig. 9 presents only a simplified electrical equivalent circuit for the two-resonator μmechanical filter of this work. In particular, a mere *LCR* circuit greatly oversimplifies the equivalent circuit for the μmechanical resonators used in the filter because it models the device as a one-port. The filter resonators are actually two-port devices, one port being at the electrode and the other being at the location of spring coupling, and forces applied to each of these ports combine to generate the overall response of a given μresonator. With this in mind, Fig. 11 presents a more suitable equivalent circuit for the overall filter, where each resonator is now modeled by the circuit of Fig. 6, and mechanical impedance transformations to the coupling spring are now conveniently modeled via transformers with turns ratios $\eta_{\rm cij}$. For the reader's convenience, expressions for all of the circuit elements are summarized along with the circuit schematic in Fig. 11.

V. Fabrication

A polysilicon surface micromachining technology similar to previously reported versions [9], [10], except for the very important distinction that the sacrificial oxide thickness in this process is only 1300 Å, was used to fabricate the μmechanical filter of this work. In this process, a series of film depositions and lithographic patterning steps—essentially identical to similar steps used in planar IC fabrication technologies—are utilized to first achieve the cross-section shown in Fig. 12(a). Here, patterned phosphorus-doped polysilicon *I/O* electrodes and interconnect (3000 Å thick) are covered by a 1300-Å-thick layer of sacrificial LPCVD silicon dioxide, except at portions wet-etched to serve as anchors for eventual resonators. A 2-μm-thick structural polysilicon film is then deposited via LPCVD at 585 °C and made conductive via a $POCl_3$ gas doping step. 5000 Å of LPCVD SiO_2 then follows to serve first as a diffusion barrier against dopant loss during a subsequent 1-h 1050 °C stress and dopant distribution anneal, then as a hard mask during patterning of the structural polysilicon layer via a chlorine-based, high-density-plasma reactive ion etch (RIE) [Fig. 12(b)]. Note that throughout the back end of this process, the sacrificial oxide layer supports the structural polysilicon material during deposition, patterning, and annealing, and defines the electrode-to-resonator gap spacing d_0. In the final step of the process, the wafer is dipped into a solution of hydrofluoric acid, which etches away the sacrificial oxide layer without significantly attacking the polysilicon structural material. This leaves the free-standing structure shown in Fig. 12(c)

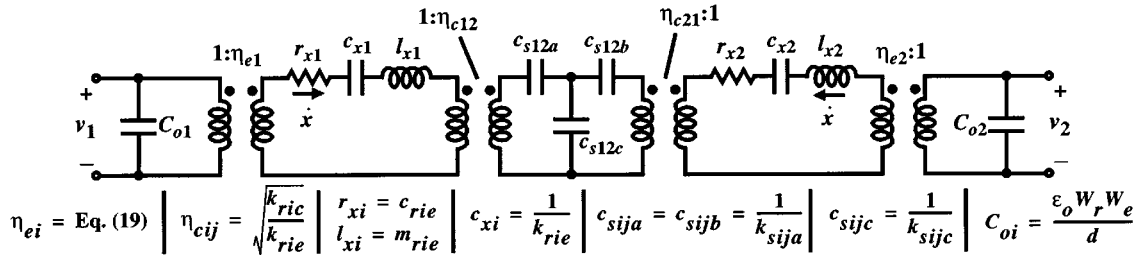

Fig. 11. Complete equivalent circuit for the micromechanical filter of Fig. 1, modeling both quarter-wavelength coupling beam design and low-velocity coupling location. Expressions for the elements are also included.

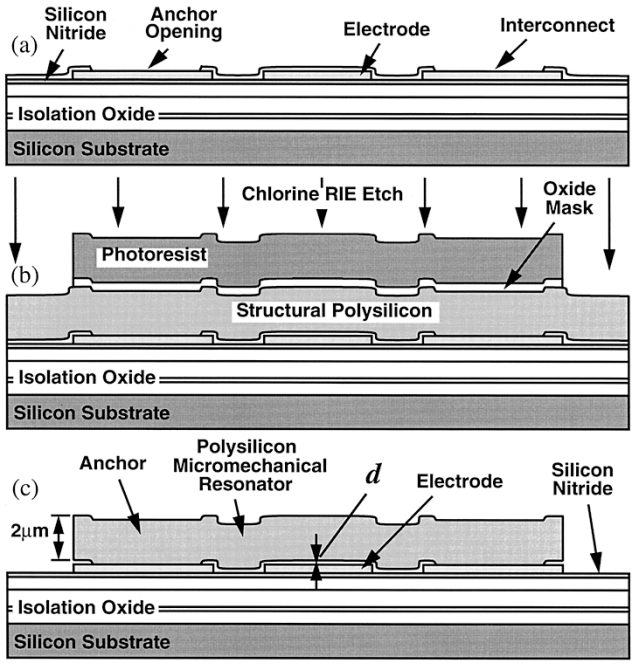

Fig. 12. Cross-sections depicting the fabrication sequence used to achieve the micromechanical filter: (a) polysilicon electrode and interconnect layers under a 1300-Å-thick sacrificial oxide, (b) required film layers and masks needed during resonator patterning in a chlorine-based RIE etch, and (c) resulting free-standing beam following a release etch in hydrofluoric acid.

free to move in several dimensions if necessary. The release etch is followed by extensive cleaning, including a 10-min dip in a solution of H_2SO_4 and H_2O_2 (i.e., piranha) and often a supercritical CO_2 clean [27], to remove etch by-products and other residuals from the thin electrode-to-resonator gap.

Micromechanical filters with center frequencies from 3 to 15 MHz were designed using the procedures detailed in Sections III and IV, then fabricated using the above polysilicon surface micromachining technology. Fig. 13 shows the scanning electron micrograph (SEM) of a fabricated filter with design specifics summarized in Table II.

VI. Experimental Results

Upon inspection and initial biasing of the completed devices, two immediate observations were made: 1) none of the devices stuck to the substrate after a standard, wet HF release and 2) pull-in voltages [8], [21] were high, on the order of 50 V, even for target resonator-to-electrode gap spacings of only 1300 Å. Both of these features result from the high spring stiffnesses required to achieve HF μmechanical resonators. The near immunity to stiction [29] and the high pull-in voltages contrast strongly with those of lower frequency applications, such as accelerometers [15], and suggests that yield loss due to these mechanisms should be substantially less for HF MEMS used for communications.

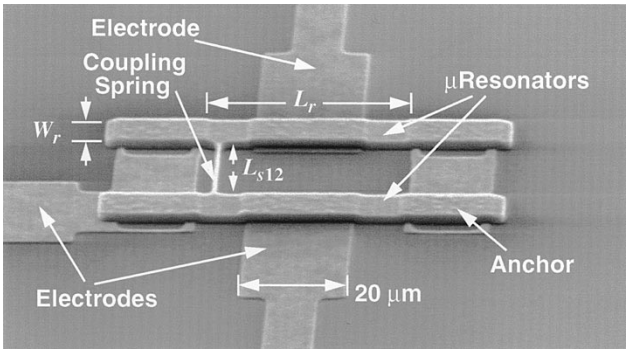

Fig. 13. SEM of a fabricated 7.81-MHz two-resonator micromechanical filter.

Since the quality factor of μmechanical resonators is large only under vacuum, resonators and filters were tested using a custom-built vacuum chamber. This chamber featured feedthroughs for connection to external instrumentation, as well as internal supports for circuit board inclusion. With this setup, the termination resistors shown in Fig. 1(a) plus buffering electronics to drive coax to external instrumentation can be placed within the vacuum chamber, alongside packaged μmechanical devices, with minimal parasitic interference. Using a mechanical pump, the minimum achievable pressure of this system was 40 mTorr.

The SEM and frequency characteristic for an 8.5-MHz parallel-plate driven, polysilicon μmechanical resonator measured using the above apparatus with no termination resistors and using a transresistance amplifier was already presented in Fig. 4. It should be mentioned that the Q of 8000 in this measurement is not as high as seen in previous polysilicon μmechanical resonators, for which Q's higher than 80 000 have been demonstrated [30]. Measurements of other resonators suggest that the lower Q for this resonator can be attributed to the use of a $POCl_3$ gas process to dope the resonator, which has been found to decrease the Q of polysilicon resonators below that of ion-implant-doped or *in situ*-doped ones [32]. Anchor dissipation may also be limiting the Q. Nevertheless, a Q of 8000 is certainly high enough to achieve extremely selective bandpass filters with minimal insertion loss.

In actual testing of filters, R_{Q2} is provided by either a matching network to an appropriate load, or by a physical

TABLE II
HF MICROMECHANICAL FILTER SUMMARY

Parameter	Value*†‡		Units
	Des./Meas.	Simulated#	
Coupling Location, l_c	4.08	**4.48**	μm
Coupling Velocity, v_c	$0.12v_{max}$	$\mathbf{0.14}v_{max}$	m/s
Center Frequency, f_o	7.81	7.81	MHz
Freq. Modification Factor, κ	(0.87915) [0.9]	0.87915	—
Bandwidth, B	18	18	kHz
Percent Bandwidth, (B/f_0)	0.23	0.23	%
Passband Ripple, PR	1.5	1.5 [0.5]	dB
Insertion Loss, IL	1.8	1.8 [1.35]	dB
20dB Shape Factor,	2.31	[2.54]	—
Stopband Rejection, SR	35	—	dB
Sp.-Free Dynamic Range, $SFDR$	~78	~78	dB
Resonator Q	8,000	**6,000**	—
Structural Layer Thickness, h	1.9	1.9	μm
μRes. Beam Length, L_r	40.8	40.8	μm
μRes. Beam Width, W_r	8	8	μm
Coupling Beam Length, L_{s12}	20.35	20.35	μm
Needed L_{s12} for λ/4	(22.47)	—	μm
Coupling Beam Width, W_{s12}	0.75	0.75	μm
Coupling Beam Stiffness, k_{s12a}	(−82.8)	−82.8	N/m
Coupling Beam Stiffness, k_{s12c}	(113.4)	113.4	N/m
Resonator Mass @ I/O, m_{re}	(5.66×10^{-13})	5.66×10^{-13}	kg
Resonator Stiffness @ I/O, k_{re}	(1,362)	1,362	N/m
Resonator Mass @ l_c, m_{rc}	(3.99×10^{-11})	2.84×10^{-11}	kg
Resonator Stiffness @ l_c, k_{rc}	(96,061)	68,319	N/m
Integrated μRes. Stiffness, k_{reff}	(1,434)	1,434	N/m
Young's Modulus, E	150	150	GPa
Density of Polysilicon, ρ	2,300	2,300	kg/m^3
Electrode-to-μRes. Gap, d_o	1,300	1,300	Å
Gap d_o Adjusted for Depletion	(1,985)	1,985	Å
Electrode Width, W_e	20	20	μm
Filter DC-Bias, V_P	35	35	V
Freq. Pulling Voltage, $V_{\Delta f}$	0.12	0	V
Q-Control Resistors, R_{Qi}	12.2 (19.6)	**14.5** [19.6]	kΩ

* Numbers in () indicate calculated or semi-empirical values.
† Bold faced numbers indicate significant deviations needed to match simulated curves with measured curves.
‡ Numbers in [] indicate values expected from an ideal simulation with no parasitics and perfect termination. The value for κ in the "Des./Meas." column was obtained via finite-element simulation using ANSYS.
\# Top 11 rows represent simulation outputs; the rest are used as inputs for simulation.

resistor with value R_{Q2} in shunt with the output node that converts i_x to a voltage that can then be buffered to subsequent circuit loads. Alternatively, transresistance detection can be implemented via an op-amp-based inverting amplifier using an input resistor with value R_{Q2}.

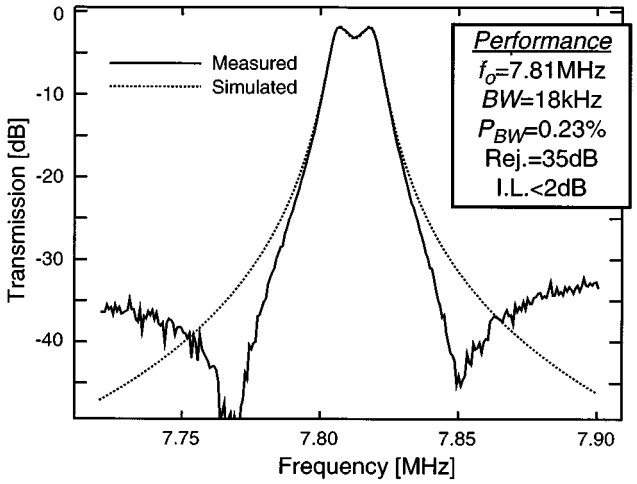

Fig. 14. Measured spectrum for a terminated 7.81-MHz μmechanical filter with excessive input/output shunt capacitance. Here, $Q_{\rm fltr} = 435$.

A. Micromechanical Filter Testing and Model Evaluation

The measured spectrum for a terminated 7.81 MHz two-resonator μmechanical filter is shown in Fig. 14 (solid curve). The bandwidth of this filter is 18 kHz, which is very close to the design value. The insertion loss is only 1.8 dB, which is impressive for a bandpass filter with a percent bandwidth of 0.23% ($Q_{\rm fltr} = 435$) and which can be attributed to the high Q of the constituent μmechanical resonators. Designed and measured μmechanical filter characteristics are summarized in Table II. It should be noted that although the analytical design calls for 19.6-kΩ termination resistors, only 12.2-kΩ resistors were used in the actual measurement to minimize phase lags caused by board-level parasitic capacitance.

In addition to the measured frequency response, Fig. 14 also presents a simulated spectrum (dotted line) using the equivalent circuit described by Fig. 11 with element values derived from the "simulated" column of Table II and summarized in Table III. This simulation attempts to mimic the measured frequency characteristic in the passband. As such, it includes shunt parasitic capacitors $C_{\rm Pi} = 100$ fF at the input and output nodes (see Fig. 1) to model board-level parasitics that interact with termination resistors $R_{\rm Qi}$ and generate increased passband ripple. It should be noted, however, that a few adjustments were necessary to attain the degree of matching shown. In particular, note that the target gap spacing of 1300 Å was not used to generate the "simulated" column in Table II, nor the values in Table III. Rather, a larger gap spacing of 1985 Å was used that accounts for depletion in the resonator beam induced by the V_P-induced electric field between the nondegenerately doped n-type beam and the n-type electrode. This value of gap spacing was semiempirically determined by matching measured plots of resonator f_0 versus V_P with simulations based on (12), using d_0 and κ as fitting parameters.

In addition, as indicated in boldface in Table II, the coupling location l_c was adjusted to match bandwidths, and the resonator Q and the filter termination resistance $R_{\rm Qi}$ were adjusted to

TABLE III
HF μMECHANICAL FILTER CIRCUIT ELEMENT VALUES

Parameter	Value	Units
Coupling Location, l_c	4.48	μm
C_{o1}=C_{o2}	7.14	fF
l_{x1}=l_{x2}	5.66×10^{-13}	H
c_{x1}=c_{x2}	0.000734	F
r_{x1}=r_{x2}	4.62×10^{-9}	Ω
c_{s12a}=c_{s12b}	−0.0121	F
c_{s12c}	0.00882	F
η_{e1}=η_{e2}	1.20×10^{-6}	C/m
η_{c12}=η_{c21}	7.08	C/m

match the measured insertion loss. In particular, the value of R_{Qi} needed to match the simulated insertion loss and passband ripple was 14.5 kΩ, not the 12.2 kΩ actually used for the measurement.

The l_c adjustment is not unreasonable, since the coupling beam has a finite width of 0.75 μm, and the exact coupling location is not necessarily at the center of the coupling beam but could be anywhere along its finite width. Furthermore, torsional motions of the coupling beam can also influence the actual mechanical coupling, thus changing the effective l_c. The adjustment in Q seen in Table II is also plausible, since a small number of resonators exhibited lower Q than the 8000 measured in Fig. 4. The small deviation in R_{Qi} also should not be alarming, given some uncertainty in the actual gap distance for this process.

Note that although the simulation matches the measurement very well in the passband, it deviates substantially in its transition to the stopband. In particular, the measured curve features loss poles not modeled by the theory of Section IV that substantially improve the shape factor of the filter. The loss poles in Fig. 14 result largely from action of the feedthrough capacitor $C_{P(fd)}$ (see Fig. 1) in a similar fashion to the introduction of loss poles via bridging capacitors in crystal filter design [26]. In the present experiment, $C_{P(fd)}$ is actually a parasitic element; i.e., loss poles were introduced inadvertently. For fully integrated filters, in which μmechanics and circuits are fabricated side-by-side on a single chip, parasitic capacitors are expected to be much smaller. In this case, the feedthrough capacitor $C_{P(fd)}$ can then be purposefully designed into the filter if loss poles are desired.

B. Low-Velocity Coupling

The low-velocity coupling design strategy detailed in Section IV was verified by measuring the bandwidths of filters as a function of coupling spring location along the resonator beam length. Fig. 15(a) and (b) compares the measured frequency characteristics for two filters, one coupled at $y_c = 10$ μm to achieve $(0.53)v_{\max}$ coupling and another at $y_c = 4.08$ μm to achieve a lower coupling velocity of $v_c = (0.12)v_{\max}$. The filter bandwidth clearly changes as the coupling location changes. In particular, the $(0.12)v_{\max}$ coupled filter exhibits a percent bandwidth of 0.23%, which is much smaller than the 2.5% of its

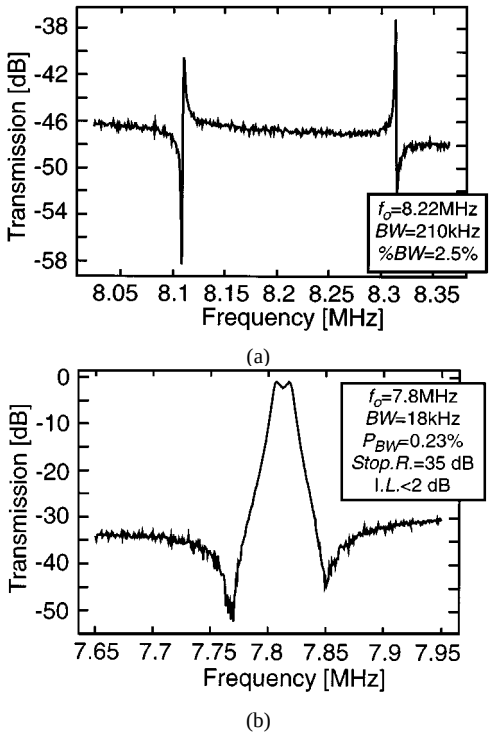

Fig. 15. Frequency characteristics for (a) a $(0.53)v_{\max}$ coupled filter and (b) a $(0.12)v_{\max}$ coupled filter, both measured under 70-mTorr pressure.

$(0.53)v_{\max}$ coupled counterpart and which verifies the utility of low velocity coupling for implementing high-Q filters on the microscale. It should be noted that the termination resistors required to flatten the passband of the $(0.53)v_{\max}$-coupled filter in Fig. 15(a) were too large for off-chip testing, where relatively large parasitic capacitors introduce passband distorting phase lags. Thus, only the unterminated spectrum is shown, and the bandwidth is taken as the frequency range between mode peaks. The actual terminated bandwidth will be slightly larger than this. In addition, the difference in the center frequencies of the two spectra arises because a smaller value of V_P was used to measure Fig. 15(a).

C. Passband Tuning

Although their *matching* tolerances are fairly good, planar fabrication technologies often exhibit rather poor *absolute* tolerances. For example, integrated capacitors in CMOS technologies can often be matched to 0.2%, but their absolute values can deviate from designed values by as much as 20% [33]. From the micromechanical perspective, the absolute resonance frequencies of micromechanical resonators can deviate from their designed values [using (12)] by several percent—as much as 3% in the University of Michigan's Solid-State Electronics Laboratory. Such frequency deviations are caused by any number of process-related phenomena, such as width W variations due to etch undercutting, thickness h variations due to film deposition rate inconsistencies, and residual stress in deposited films, to name a few. As with planar IC technologies, these variations still seem to be uniform in small areas, so resonator-to-resonator frequency matching tolerances are fairly good, on the order of 0.4%.

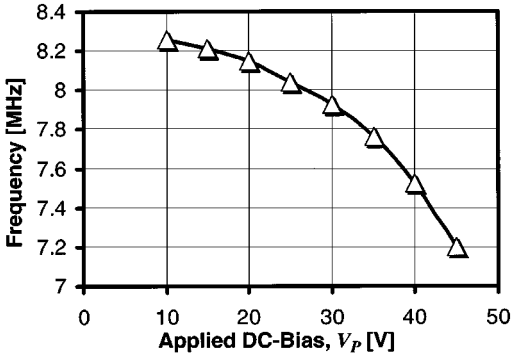

Fig. 16. Measured frequency versus applied dc bias V_P for a parallel-plate transduced clamped–clamped beam μmechanical resonator.

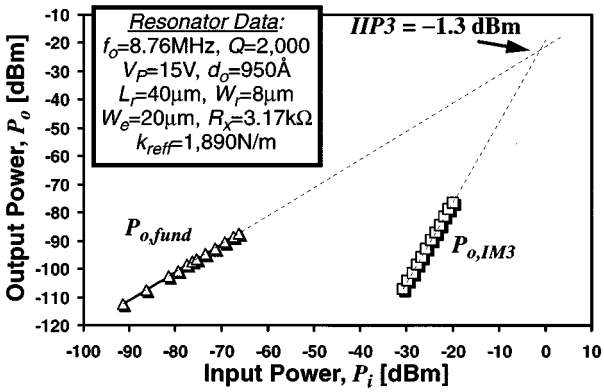

Fig. 17. Measured output power P_0 versus input power P_i plot for determination of IIP3 for an 8.76-MHz μmechanical resonator. Input tones for IM_3 determination are spaced 200 and 400 kHz from the resonator center frequency.

From a filter perspective, assuming identical resonators are used, the above implies that filter passbands should be fairly repeatable, at least for low $Q_{\rm fltr}$ designs. However, absolute tolerances will cause center frequencies to deviate significantly from designed values. In addition, for filters with high $Q_{\rm fltr}$, even small mismatches in resonator frequency can cause significant passband distortion. Thus, for the majority of applications, some form of trimming or tuning is required to achieve accurate passband shape and location.

As indicated by (3), some amount of voltage-controlled frequency tuning is available via adjustment of the dc-bias voltage V_P. Fig. 16 shows a plot of frequency versus V_P for a clamped–clamped beam μresonator designed to the specifications of Table II. Here, a 9.4% tuning range is provided over 30 V of bias variation. As seen from (12)–(15), the tuning range is strongly dependent upon resonator design, increasing with decreasing gap spacing and decreasing with increasing stiffness.

To correct the passband of a micromechanical filter suffering from mismatched resonators, the $V_{\Delta f}$ voltage in Fig. 1 is simply varied to adjust the resonance frequency of *Resonator1* until it matches that of *Resonator2*, at which point passband distortion is removed. From Table II, a tuning voltage $V_{\Delta f}$ of 0.12 V was required to attain Fig. 14. Although not used in this design, separate tuning electrodes could also be introduced alongside the I/O electrode of each resonator to decouple the frequency tuning function from the I/O.

For practical purposes, depending upon how well process variations can be controlled, the range of V_P-activated frequency tuning may not be adequate for all cases. This will be especially true in portable systems, which generally operate with low supply voltages (below 3 V) that leave little room for V_P variation, at least not enough to correct for absolute tolerances as high as 3%. For these cases, alternative trimming technologies are being investigated that, when combined with V_P-activated tuning, should enable a wide range of precise frequency adjustment [32].

D. Spurious-Free Dynamic Range

Pursuant to measurement of the out-of-band SFDR for a μmechanical filter, Fig. 17 presents a plot of output power P_0 versus input power P_i for an 8.76-MHz polysilicon μmechanical resonator in series with a resistor $R_p = 3050\ \Omega$, with design and operating data also given. Output power responses to both an in-band input signal at $f_0 = 8.76$ MHz and a two-tone out-of-band signal with tones spaced 200 and 400 kHz away from f_0 are plotted and indicated as $P_{0,\,fund}$ and $P_{0,\,IM3}$, respectively. It should be noted that these plots were measured from a stand-alone, one-port resonator (as opposed to a properly terminated filter), and thus, the output was not matched to the measurement apparatus (a spectrum analyzer). This lack of matching leads to more insertion loss than normally seen in a matched filter, but does not invalidate an third-order input intercept point (IIP3) determination based on this data. In particular, the IIP3 derives from an in-band IM_3 input force component generated by input transducer nonlinearity and is not a function of output matching. (In fact, the x-axis of Fig. 17 would perhaps be better construed as velocity power, rather than electrical.) Thus, despite the lack of output matching, IIP3 can still be extracted from Fig. 17 and is seen to be -1.3 dBm.

Again, since IIP3 is a function of input velocity power, the data of Fig. 17 can be extended to a properly terminated filter by matching displacements induced by electrical input power. Since velocity corresponds essentially to the current flowing through the equivalent circuit of a resonator, the P_0 versus P_i plot for a properly terminated filter using the 8.76-MHz resonator described above can be obtained from Fig. 17 by shifting the P_i-axis so that P_i values for the filter correspond to the same resonator currents as generated by P_i's for the stand-alone resonator in Fig. 17. This can be done using the expression

$$P_{i,\,fltr} = \left(\frac{2(R_{\rm Qi}R_x)}{(R_x + R_p)}\right) P_{i,\,\rm res} \tag{39}$$

where $P_{i,\,fltr}$ and $P_{i,\,\rm res}$ are the input power scales for the filter and resonator plots, respectively. Using (39), assuming a 36-kHz bandwidth filter centered at 8.76 MHz using the resonator and bias values of Fig. 17 with $R_{\rm Qi} = 10\,\rm k\Omega$, then shifting all curves upwards to reflect the 2-dB insertion loss seen in Fig. 14, yields Fig. 18. The IIP3 point for this extrapolated filter is now 5.1 dBm.

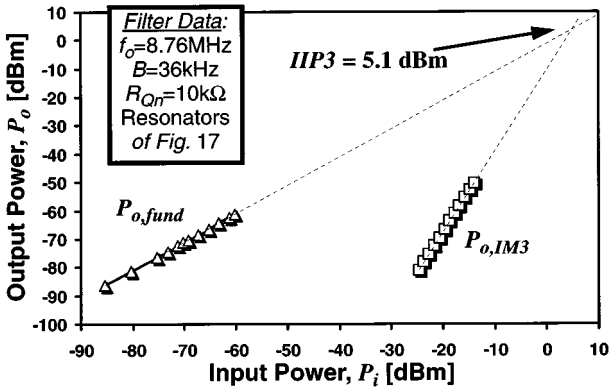

Fig. 18. Output power P_0 versus input power P_i plot for determination of IIP3 for an 8.76-MHz μmechanical filter (extrapolated from Fig. 17).

The out-of-band SFDR (with tones 200 and 400 kHz offset from the filter center frequency) can now be determined via the expression [31]

$$\text{SFDR} = \tfrac{2}{3}(\text{IIP3} - N_{\text{oi}}) - \text{SNR}_{\min} \tag{40}$$

where all quantities are in decibels, $\text{SNR}_{\min}$ is the required minimum signal-to-noise ratio, and N_{oi} is the input-referred noise power, given for this filter by

$$N_{\text{oi}} = N_{\text{RQ}} + IL + 10 \log B \tag{41}$$

where $N_{\text{RQ}} = -174$ dBm is the thermal noise power delivered by R_Q into a matched load, IL is the insertion loss of the filter, and B is the filter bandwidth. Note that noise associated with Brownian motion of the μmechanical filter structure is modeled by thermal noise in its R_x's [10], and is included in the IL component of (41). For $IL = 2$ dB and $\text{SNR}_{\min} = 10$ dB, (40) yields an SFDR $= 78$ dB.

VII. Frequency Range of Applicability

The ultimate frequency range of the described micromechanical resonators is of great interest and is presently a topic under intense study. From a purely geometric standpoint, the frequency range of micromechanical resonators can extend well into the gigahertz range. For example, the dimensions of a clamped–clamped beam resonator required to attain a frequency of 1 GHz are (referring to Fig. 3 and assuming $V_P = 0$ V) approximately $L_r \approx 4$ μm, $W_r = 2$ μm, and $h = 2$ μm, where finite-element analysis should be used to account for width and anchoring effects. This frequency can also be attained by longer beams vibrating in higher modes. Thus, according to analytical and finite-element prediction, frequencies into the gigahertz range are geometrically possible.

Geometry, however, is only one of many important considerations. The applicable frequency range of micromechanical resonators will also be a function of several other factors, including:

1) quality factor, which may change with frequency for a given material, depending upon frequency-dependent energy loss mechanisms [28];
2) series motional resistance R_x (cf., Fig. 11), which must be minimized to allow R_{Qi} impedance matching with other transceiver components and to alleviate filter passband distortion due to parasitics [14], [34], [35];
3) absolute and matching tolerances of resonance frequencies, which will both be functions of the fabrication technology and of frequency trimming or tuning strategies [32];
4) stability of the resonance frequency against temperature variations, mass loading (e.g., by contaminant molecules [36]), aging, and other environmental phenomena.

Each of the above phenomena is currently under study. In particular, assuming adequate vacuum can be achieved, the ultimate quality factor will be strongly dependent upon the material type, and even the manufacturing process. For example, surface roughness or surface damage during fabrication may play a role in limiting quality factor. In fact, preliminary results comparing the quality factor achievable in boron-source-doped polysilicon structures (which exhibit substantial pitting of the poly surface) versus implant-doped ones, indicate that the latter exhibit almost an order of magnitude higher Q at frequencies near 10 MHz. Another loss mechanism that may become more important with increasing frequency is loss to the substrate through anchors. More balanced tuning fork designs could alleviate this mechanism.

From a filter design perspective, the practical frequency range is limited by electromechanical coupling. In particular, electromechanical coupling largely determines the value of R_{Qi} required to terminate a given filter, and thus, dictates matching requirements, power-handling capability, and susceptibility to passband distorting shunt parasitic capacitance C_{Pi}. To satisfy present-day impedance matching requirements, a small R_{Qi} is often required, which from (24) necessitates a small value of R_x in the resonators making up a given filter. From (18), this is most conveniently achieved by reducing the electrode-to-resonator gap spacing d_0, increasing the electrode-to-resonator area overlap area $A_0 = W_r W_e$, or increasing the dc bias voltage V_P applied to the resonator. For practical purposes, A_0 is limited by the total beam length (which is in turn dictated by f_0), and V_P is limited by the available power supply or by the highest voltage achievable via charge pumping in the circuit technology being used. Reduction of the electrode-to-resonator gap spacing, perhaps down to 200 Å rather than 1300 Å, and the use of different dopings for the resonator and electrode (e.g., p-type resonator, n-type electrode) to prevent depletion-based gap increases, may be the most practical methods for reducing R_x. For the filter of Fig. 13, a gap spacing of $d_0 = 276$ Å would allow the use of 1-kΩ termination resistors with $V_P = 5$ V.

Because the gap spacing for the above HF filter is defined by an oxide spacer thickness, it can be made very small, on the order of tens to hundreds of angstroms. For this reason, the minimum gap spacing is likely not determined by process limitations, but rather by dynamic range and linearity considerations. In particular, for a given displacement amplitude, a decrease in gap spacing d_0 leads to an increase in capacitive transducer nonlinearity.

This can most readily be seen in an expression for nonlinear distortion. An approximate expression for the magnitude of the in-band force component at ω_0 arising from third-order intermodulation of two out-of-band interferers at $\omega_1 = \omega_0 + \Delta\omega$

and $\omega_2 = \omega_0 + 2\Delta\omega$ can be derived by considering nonlinearities in the input capacitive transducer. Assuming that resonator displacements are small enough that stiffening nonlinearity can be neglected, such a derivation yields

$$F_{IM_3} = V_i^3 \cdot \left\{ \frac{1}{4} \frac{(\varepsilon_0 A_0)^2}{d_0^5} \frac{V_P}{k_{\text{reff}}} [2\Theta_1 + \Theta_2] + \frac{3}{4} \frac{(\varepsilon_0 A_0)^3}{d_0^8} \frac{V_P^3}{k_{\text{reff}}^2} \Theta_1 [\Theta_1 + 2\Theta_2] + \frac{3}{2} \frac{(\varepsilon_0 A_0)^4}{d_0^{11}} \frac{V_P^5}{k_{\text{reff}}^3} \Theta_1^2 \Theta_2 \right\} \quad (42)$$

where $\Theta_1 = \Theta(\omega_1)$, $\Theta_2 = \Theta(\omega_2)$, and

$$\Theta(\omega) = \frac{1}{|1 - (\omega/\omega_{u3\text{ dB}})^2 + j\omega/(Q\omega_{u3\text{ dB}})|} \quad (43)$$

where $\omega_{u3dB} = \omega_o + B/2$ is the 3-dB frequency at the upper edge of the filter passband. For the μresonator in series with $R_p = 3050\ \Omega$ of Fig. 17, (4) and (42) combine to predict an IIP3$= -1.0$ dBm, which is close to the measured value. For the parameters used in the filter example of Fig. 18, (40)–(42) yield IIP3$= 5.3$ dBm and SFDR$= 78$ dB—very close to measured/extracted values.

Equation (42) indicates that third-order intermodulation force components can be reduced by increasing the electrode-to-resonator gap spacing d_0 and the effective integrated resonator stiffness k_{reff}, while decreasing the electrode-to-resonator overlap area A_0 and the applied dc bias V_P. Unfortunately, as seen from (18) and (24), these adjustments also increase the required value of termination resistance R_{Qi}. Thus, for the filter design of this work, there is a tradeoff between linearity (i.e., dynamic range) and the ability to match to small impedances. Although small impedances are not normally required at IF frequencies, they are often needed at RF in the transmit path, e.g., to load power amplifiers. Nevertheless, even with d_0 reductions to maintain adequately low R_{Qi}, (42) predicts fairly good dynamic range at higher frequencies. For example, for a hypothetical 200-kHz bandwidth, 70-MHz μmechanical filter with $R_{\text{Qi}} = 2$ kΩ, and using μresonators with $\{Q = 8000$, $L_r = 15.2\ \mu$m, $W_r = 8\ \mu$m, $W_e = 12.2\ \mu$m, $h = 2\ \mu$m, $d_0 = 203$ Å, $k_{\text{reff}} = 64\,152$ N/m, and $R_x = 186\ \Omega$ for $V_P = 6$ V$\}$, (40), (42), and the design equations of Sections III and IV yield (with input tones offset 400 and 800 kHz from f_0) IIP3$= 12$ dBm and an out-of-band SFDR of 78 dB.

From a broader perspective, the above linearity versus impedance tradeoff amounts essentially to a power-handling limitation. Some of the more promising methods for enhancing the power-handling capability of micromechanical filters include alternative transducer configurations (e.g., more linear capacitive transduction, or piezoelectric transduction) and various system-level solutions (e.g., paralleling micromechanical filters), both of which are the subject of current research.

VIII. Conclusions

Surface-micromachined, polysilicon, high-Q μmechanical bandpass filters in the HF range have been designed, fabricated, and tested with particular attention to design limitations caused by miniaturization of resonator and spring elements. In particular, coupling beam masses are comparable to those of resonators on this microscale, so mass loading effects are amplified in this domain. In the absence of proper design methodologies, such mass loading can generate center frequency shifts and distortion in the filter passband. To suppress this effect, quarter-wavelength coupling springs are utilized, but these place constraints on the values of coupler stiffness that then limit the percent bandwidth attainable by microscale mechanical filters using a rigid geometry. A novel technique based on low-velocity coupling was introduced and demonstrated that alleviates percent bandwidth restrictions and allows the realization of high-Q μmechanical filters.

High-Q performance was demonstrated for both single μresonators and filters in the HF range, leading to impressively low insertion loss in small percent bandwidth micromechanical filters. Passband distortion caused by finite planar process tolerances was alleviated via a voltage-controlled frequency pulling capability arising from effective electrical stiffnesses that add to the mechanical stiffnesses of the resonator beams. Such frequency tuning or trimming methods are expected to become increasingly important as dimensions shrink to accommodate higher VHF and UHF frequencies.

Acknowledgment

The authors would like to thank the staff of the University of Michigan's Solid-State Laboratory for fabrication support.

References

[1] H. Khorramabadi and P. R. Gray, "High-frequency CMOS continuous-time filters," *IEEE J. Solid-State Circuits*, vol. SC-19, pp. 939–948, Dec. 1984.

[2] R. A. Sykes, W. L. Smith, and W. J. Spencer, "Monolithic crystal filters," in *1967 IEEE Int. Conv. Rec. pt. II*, Mar. 20–23, pp. 78–93.

[3] R. C. Rennick, "An equivalent circuit approach to the design and analysis of monolithic crystal filters," *IEEE Trans. Sonic Ultrason.*, vol. SU-20, pp. 347–354, Oct. 1973.

[4] C. K. Campbell, *Surface Acoustic Wave Devices for Mobile Wireless Communications*. New York, NY: Academic, 1998.

[5] A. A. Abidi, "Direct-conversion radio transceivers for digital communications," *IEEE J. Solid-State Circuits*, vol. 30, pp. 1399–1410, Dec. 1995.

[6] J. C. Rudell, J.-J. Ou, T. B. Cho, G. Chien, F. Brianti, J. A. Weldon, and P. R. Gray, "A 1.9-GHz wide-band IF double conversion CMOS receiver for cordless telephone applications," *IEEE J. Solid-State Circuits*, vol. 32, pp. 2071–2088, Dec. 1997.

[7] D. H. Shen, C.-M. Hwang, B. B. Lusignan, and B. A. Wooley, "A 900-MHz RF front-end with integrated discrete-time filtering," *IEEE J. Solid-State Circuits*, vol. 31, pp. 1945–1954, Dec. 1996.

[8] R. T. Howe and R. S. Muller, "Resonant microbridge vapor sensor," *IEEE Trans. Electron Devices*, vol. ED-33, pp. 499–506, 1986.

[9] W. C. Tang, T.-C. H. Nguyen, and R. T. Howe, "Laterally driven polysilicon resonant microstructures," *Sensors Actuators*, vol. 20, pp. 25–32, 1989.

[10] C. T.-C. Nguyen and R. T. Howe, "An integrated CMOS micromechanical resonator high-Q oscillator," *IEEE J. Solid-State Circuits*, vol. 34, pp. 440–445, Apr. 1999.

[11] ——, "Microresonator frequency control and stabilization using an integrated micro oven," in *Dig. Tech. Papers 7th Int. Conf. Solid-State Sensors and Actuators (Transducers'93)*, Yokohama, Japan, June 7–10, 1993, pp. 1040–1043.

[12] C. T.-C. Nguyen, "Frequency-selective MEMS for miniaturized low-power communication devices," *IEEE Trans. Microwave Theory Tech.*, vol. 47, no. 8, pp. 1486–1503, Aug. 1999.

[13] C. T.-C. Nguyen, L. P. B. Katehi, and G. M. Rebeiz, "Micromachined devices for wireless communications," *Proc. IEEE*, vol. 86, pp. 1756–1768, Aug. 1998.

[14] K. Wang and C. T.-C. Nguyen, "High-order micromechanical electronic filters," in *Proc. 1997 IEEE Int. Micro Electro Mechanical Systems Workshop*, Nagoya, Japan, Jan. 26–30, 1997, pp. 25–30.
[15] B. E. Boser and R. T. Howe, "Surface micromachined accelerometers," *IEEE J. Solid-State Circuits*, vol. 31, pp. 366–375, Mar. 1996.
[16] N. Yazdi, F. Ayazi, and K. Najafi, "Micromachined inertial sensors," *Proc. IEEE*, vol. 86, pp. 1640–1659, Aug. 1998.
[17] S. Bouwstra and B. Geijselaers, "On the resonance frequencies of microbridges," in *Dig. Tech. Papers 6th Int. Conf. Solid-State Sensors and Actuators*, San Francisco, CA, June 24–27, 1991, pp. 538–542.
[18] Q. Meng, M. Mehregany, and R. L. Mullen, "Theoretical modelling of microfabricated beams with elastically restrained supports," *J. Microelectromech. Syst.*, vol. 2, no. 3, pp. 128–137, Sept. 1993.
[19] W. E. Newell, "Miniaturization of tuning forks," *Science*, vol. 161, pp. 1320–1326, Sept. 1968.
[20] R. A. Johnson, *Mechanical Filters in Electronics*. New York, NY: Wiley, 1983.
[21] H. Nathanson, W. E. Newell, R. A. Wickstrom, and J. R. Davis Jr., "The resonant gate transistor," *IEEE Trans. Electron Devices*, vol. ED-14, pp. 117–133, Mar. 1967.
[22] H. A. C. Tilmans, "Equivalent circuit representation of electromechanical transducers: I. Lumped-parameter systems," *J. Micromech. Microeng.*, vol. 6, pp. 157–176, 1996.
[23] H. A. C. Tilmans and R. Legtenberg, "Electrostatically driven vacuum-encapsulated polysilicon resonators: Part II. Theory and performance," *Sensors and Actuators*, vol. A45, pp. 67–84, 1995.
[24] A. I. Zverev, *Handbook of Filter Synthesis*. New York: Wiley, 1967.
[25] M. Konno and H. Nakamura, "Equivalent electrical network for the transversely vibrating uniform bar," *J. Acoust. Soc. Amer.*, vol. 38, pp. 614–622, Oct. 1965.
[26] M. S. Lee, "Polylithic crystal filters with loss poles at finite frequencies," in *Proc. 1975 IEEE Int. Symp. Circuits and Syst.*, Apr. 21–23, 1975, pp. 297–300.
[27] G. T. Mulhern, D. S. Soane, and R. T. Howe, "Supercritical carbon dioxide drying of microstructures," in *Proc. 7th Int. Conf. Solid-State Sensors and Actuators (Transducers'93)*, Yokohama, Japan, June 1993, pp. 296–299.
[28] V. B. Braginsky, V. P. Mitrofanov, and V. I. Panov, *Systems with Small Dissipation*. Chicago, IL: Univ. Chicago Press, 1985.
[29] C. H. Mastrangelo and C. H. Hsu, "Mechanical stability and adhesion of microstructures under capillary forces—Part I: Basic theory," *J. Microelectromech. Syst.*, vol. 2, no. 1, pp. 33–43, 1993.
[30] C. T.-C. Nguyen and R. T. Howe, "Quality factor control for micromechanical resonators," in *Tech. Dig. IEEE Int. Electron Devices Meeting*, San Francisco, CA, Dec. 14–16, 1992, pp. 505–508.
[31] B. Razavi, *RF Microelectronics*. Englewood Cliffs, NJ: Prentice-Hall, 1998.
[32] K. Wang, A.-C. Wong, W.-T. Hsu, and C. T.-C. Nguyen, "Frequency-trimming and Q-factor enhancement of micromechanical resonators via localized filament annealing," in *Dig. Tech. Papers 1997 Int. Conf. Solid-State Sensors and Actuators*, Chicago, IL, June 16–19, 1997, pp. 109–112.
[33] R. Gregorian and G. C. Temes, *Analog MOS Integrated Circuits for Signal Processing*. New York: Wiley, 1986.
[34] F. D. Bannon III. and C. T.-C. Nguyen, "High frequency microelectromechanical IF filters," in *Tech. Dig. 1996 IEEE Electron Devices Meeting*, San Francisco, CA, Dec. 8–11, 1996, pp. 773–776.
[35] J. R. Clark, A.-C. Wong, and C. T.-C. Nguyen, "Parallel-resonator HF micromechanical bandpass filters," in *Dig. Tech. Papers 1997 Int. Conf. Solid-State Sensors and Actuators*, Chicago, IL, June 16–19, 1997, pp. 1161–1164.
[36] C. T.-C. Nguyen and R. T. Howe, "Design and performance of monolithic CMOS micromechanical resonator oscillators," in *Proc. 1994 IEEE Int. Frequency Control Symp.*, Boston, MA, May 31 –June 3, 1994, pp. 127–134.

Frank D. Bannon III (S'94–M'98) received the B.S. degree from Pennsylvania State University, University Park, in 1995 and the M.S. degree from the University of Michigan, Ann Arbor, in 1997, both in electrical engineering.

Since 1997, he has been a Member of Technical Staff at Lucent Technologies' Bell Laboratories, Holmdel, NJ. His interests are in RF and microwave analog circuit design and MEMS for optics and signal-processing applications.

Mr. Bannon is a member of HKN and Phi Kappa Phi.

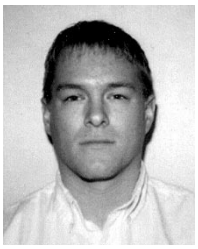

John R. Clark (S'99) was born in Dearborn, MI, in 1974. He received the B.S. and M.S. degrees in electrical engineering from the University of Michigan, Ann Arbor, in 1996 and 1998, respectively, where he is currently pursuing the Ph.D. degree.

His research is on high-frequency micromechanical filters.

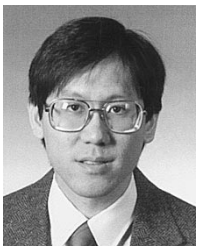

Clark T.-C. Nguyen (S'90–M'95) was born in Austin, TX, on March 29, 1967. He received the B.S., M.S., and Ph.D. degrees from the University of California at Berkeley in 1989, 1991, and 1994, respectively, all in electrical engineering and computer sciences.

In 1995, he joined the Faculty of the University of Michigan, Ann Arbor, where he is currently an Assistant Professor in the Department of Electrical Engineering and Computer Science. From 1995 to 1997, he was a Member of the National Aeronautics and Space Administration (NASA)'s New Millennium Integrated Product Development Team on Communications, which roadmaps future communications technologies for NASA use into the turn of the century. His research interests focus upon microelectromechanical systems and include integrated micromechanical signal processors and sensors, merged circuit/micromechanical technologies, RF communication architectures, and integrated circuit design and technology.

Prof. Nguyen received the 1938E Award for Research and Teaching Excellence from the University of Michigan in 1998 and an EECS Departmental Achievement Award in 1999. He was a Finalist for the 1998 Discover Magazine Technological Innovation Awards. Together with his students, he received the Roger A. Haken Best Student Paper Award at the 1998 IEEE International Electron Devices Meeting and the Judges Award for Best Paper at the 1998 IEEE MTT-S International Microwave Symposium. He recently Cochaired the Workshop on Microelectromechanical Devices for RF Systems at the 1999 IEEE MTT-S Symposium.